Electronic Supplementary Information

METHODS

Scanning electron microscopy

To verify membrane surface and cross-sectional homogeneity, a scanning electron microscope (FEI NOVA nanoSEM Field Emission) was used to image the surface and edge of the laminated nitrocellulose membrane at magnifications of 1000X, 1500X, and 5000X. Images of 400 nm green fluorescent nanoparticles (ThermoFisheR) were also taken using cryo-SEM on the same instrument. Samples were mounted on specimen holders (Gatan) and plunge frozen in slushed liquid nitrogen. When bubbling stopped, samples were cryo-transferred into the preparation chamber (Gatan) for fracture, if applicable. For samples that were not fractured, the samples were transferred into the SEM cryo stage for sublimation at -90°C until areas of interest were visible. Next, samples were returned to a -180°C chamber for sputter coating for 2 minutes with a platinum target. After sputter coating, the samples were transferred back to the SEM stage and imaged at 5 kV/spot size 3 at -140°C. The nanoparticles were imaged both independently on a metal mount (not fractured) and within the nitrocellulose membrane (fractured) to elucidate the relationship between the size of the nanoparticles and the size of the membrane pores.

To estimate the average pore size of the AE99 nitrocellulose, the "Analyze Particles" feature in ImageJ was used according to the methods described by Linnes and colleagues.[42]

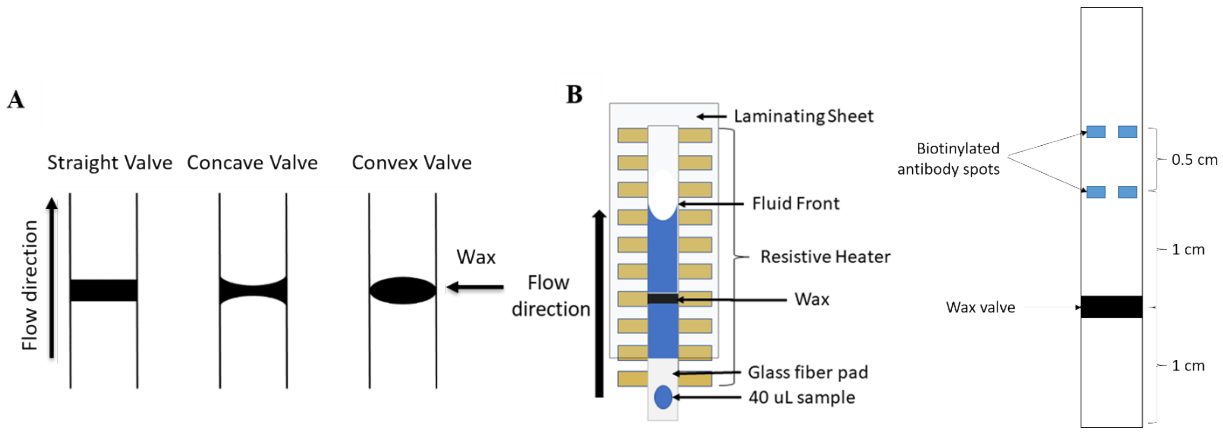

Scheme S1: A. Different valve geometries. B. Experimental setup for macroscopic flow analysis. C. Model triplex LFIA with wax valves and biotinylated goat antibody test and control spots

COMSOL governing equations

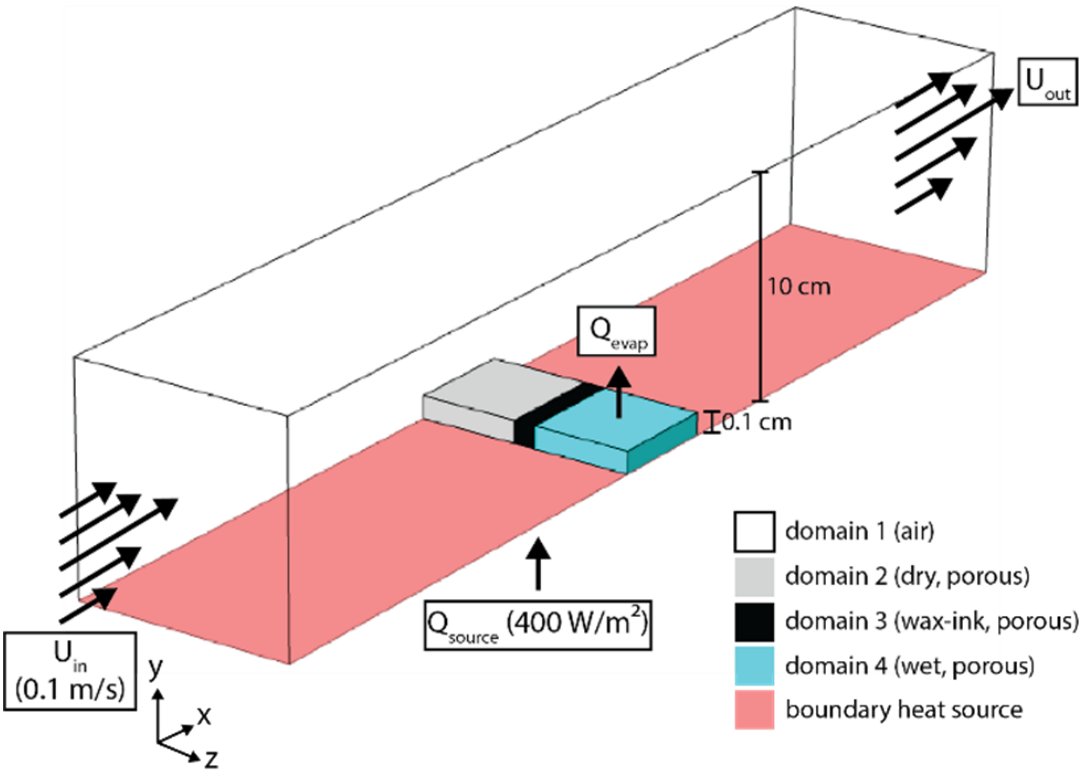

Scheme S2: Schematic of model of heat transfer in wax valve in porous media. A boundary heat source simulates a thin film heater and heat loss accounted for by convective heat flux of ambient air in laminar flow and evaporative heat loss.

Table S1: COMSOL parameters to simulate the heating of a wax valve.

Parameter	**Value**	**Source**
ambient pressure	1 atm	estimated
ambient temperature	293.15 K	estimated
free stream velocity	0.1 m/s	estimated
initial water saturation in domain 4	0.5	estimated
thermal conductivity of cellulose	0.09 W/(m*K)	[44]
porosity of cellulose	0.8	[45]
permeability of cellulose	$1x10^{-15}$ m^2	[45]
heat capacity of cellulose	1650 J/(kg*K)	[46]
density of cellulose	1528 kg/m^3	[45]
thermal conductivity of wax-ink	0.18 W/(m*K)	[47]
heat capacity of wax-ink	2250 J/(kg*K)	[47]
density of wax-ink	820 kg/m^3	[47]
boundary heat source	400 W/m^2	[48]

Briefly, heat transfer was coupled to laminar flow in the porous medium domain using the non-isothermal flow interface.[49] This coupling is commonly used to describe slow flow environments and allows for the fluid density to fluctuate with temperature (as occurs in this model because of the multiphase flow of water vapor and liquid water during evaporation).[43] The governing heat transfer equation includes convection and conduction (Equation 1):

$$\rho c_p u \cdot \nabla T + \nabla \cdot q = Q + Q_p + Q_{vd} \qquad \text{Equation 1}$$

where ρ describes the fluid density, c_p describes specific heat, $\boldsymbol{u}$ is velocity, T describes temperature, Q accounts for heat from the boundary source and latent heat of evaporation, Q_p accounts for work done by pressure changes caused by the compressible flow, Q_{vd} accounts for heat from viscous dissipation, and $\boldsymbol{q}$ is described by Equation 2:

$$q = -k_{\text{eff}} \nabla T \qquad \text{Equation 2}$$

where k describes the thermal conductivity. Notably, the thermal conductivity in the porous domain (Equation 3)

$$k_{\text{eff}} = \theta_p k_p + (1 - \theta_p) k + k_{disp} \qquad \text{Equation 3}$$

is dependent on the solid volume fraction in the porous cellulose medium, θ_p, the thermal conductivity of the cellulose, k_p, the thermal conductivity of the wax-ink or water and water vapor, k, and thermal conductivity from dispersion in porous media, k_{disp}.

In the ambient air domain, there is only transport of moist air and the velocity is solved by the Navier-Stokes equation (Equation 4):

$$\underbrace{\rho\left(\frac{\partial \mathbf{u}}{\partial t} + \mathbf{u} \cdot \nabla \mathbf{u}\right)}_{1} = \underbrace{-\nabla p}_{2} + \underbrace{\nabla \cdot \left(\mu(\nabla \mathbf{u} + (\nabla \mathbf{u})^T) - \frac{2}{3}\mu(\nabla \cdot \mathbf{u})\mathbf{I}\right)}_{3} + \underbrace{\mathbf{F}}_{4} \qquad \text{Equation 4}$$

where u is velocity, p is pressure, ρ is density, μ is fluid dynamic viscosity accounting for 1) inertial forces, 2) pressure forces, 3) viscous forces. This is solved with the continuity equation $\nabla \cdot (\rho \boldsymbol{u}) = 0$.

Within the porous domain, there is two-phase flow of water vapor and liquid water. The Brinkman equation, an extension of Darcy's Law, is used for the gaseous vapor phase because it more accurately describes fast flow within a porous domain while Darcy's Law is used to describe the slower flow, liquid phase water, within the porous membrane.

Microscale Particle flow

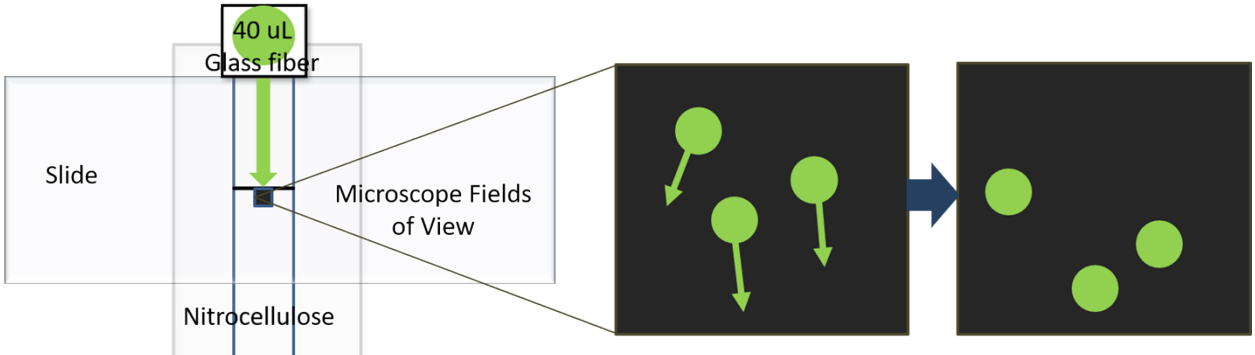

Scheme S3: Diagram of microscope setup for imaging particle flow in the nitrocellulose membrane.

RESULTS

Membrane and valve analysis

SEM was used to validate underlying assumptions necessary for the methods used. The nitrocellulose membrane used in the macroscopic and microscopic analyses was imaged to substantiate the underlying assumptions in our models. Surface (Figure 1A) and cross-sectional (Figure 1B) membrane homogeneity in pore size, with an estimated average pore diameter of 4.4 µm (data not shown), indicate that the conclusions derived from analyzing particle motion should be valid across all dimensions of the membrane, justifying the validity of using the Richards equation in our quantitative fluid analysis. Analysis of a 5000X SEM nitrocellulose image in ImageJ resulted in. The Richards equation used to model flow in unsaturated porous media is based only on properties of the material itself and does not make any assumptions about the shape or size of the pores, considering only average properties.[50] From the SEM images, it is reasonable to conclude that the average material properties are uniform across the entire membrane, so the Richards equation is also a reasonable model of flow in the nitrocellulose membranes.

Additionally, wax melted into the nitrocellulose membrane was imaged on its surface (Figure 1C) and through its cross-section (Figure 1D), demonstrating complete obstruction of the membrane pores and indicating that fluid would only be able to pass through the valves if the solid barrier formed by the wax was compromised. Finally, images of the 400 nm fluorescent nanoparticles used in µPIV flow analysis revealed their shape and size (Figure 1E) compared to the shape and size of the membrane's pores (Figure 1F), demonstrating the ability of the particles to travel freely and easily throughout the membrane as an adequate representation of fluid flow patterns.

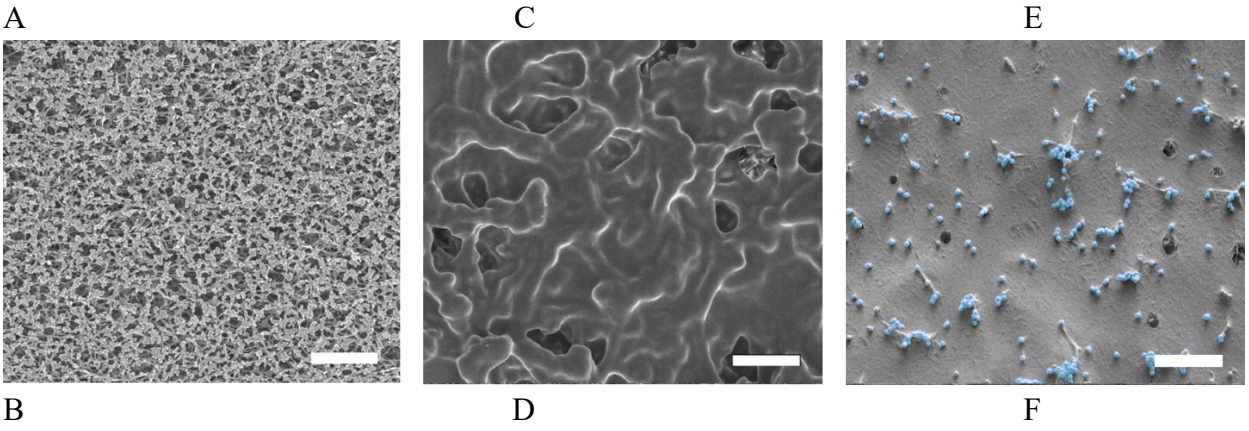

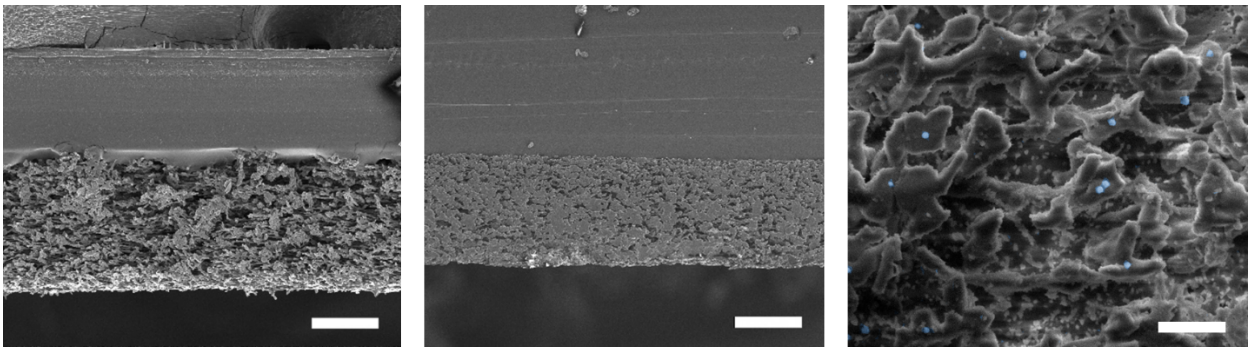

Figure S1: SEM (A-D) and Cryo-SEM (E, F) images. (A) SEM image of surface of nitrocellulose membrane (1000X magnification, scale bar = 50 µm). (B) Image of cross-section through nitrocellulose membrane demonstrating homogeneity of pore structure throughout membrane depth (1000X magnification, scale bar = 50 µm). (C) SEM of nitrocellulose membrane with wax melted throughout (5000X magnification, scale bar = 10 µm). (D) SEM image of cross-section of nitrocellulose membrane with wax melted throughout (1000X magnification, scale bar = 50 µm). (E) Cryo-SEM of 400 nm nanoparticles (5000X magnification, scale bar = 10 µm). (F) Cryo-SEM of 400 nm nanoparticles in a cross section of the nitrocellulose membrane (5000X magnification, scale bar = 10 µm). Selected particles colored blue for ease of visualization in E and F.

A key takeaway from the cryo-SEM images is the size of the particles in relation to the size of the membrane pores. Supporting our analysis of pore size described previously, in Figure 1F, it is apparent that the both the 400 nm and 100 nm particles are more than 10 times smaller than the average size of cavities within the nitrocellulose membrane through which they flow. However, particles can still become trapped in areas where pores are obstructed or when the material forms pores that are too small for the particles to pass through. Indeed, some particles were frequently observed to become stuck during experimentation, especially in less homogenous areas of the membrane, such as the edges. Nevertheless, for the purposes of this analysis, the size relation between the particles and the membrane pores was sufficient to assume that the particles aligned with the bulk transport patterns of the fluid reasonably well.

Radiation effects

Radiation between two bodies, such as a thin film heater and a test strip, can be modified from the Stefan-Boltzmann Law to $\Delta E = \in_{eff} \sigma A F_{A\to B}(T_A^4 - T_B^4)$ where ΔE is the heat transfer rate, $\in_{eff}$ is the emissivity, σ is the Stefan-Boltzmann constant, A is the surface area, F is the view factor, and T is the temperature of the bodies. Assuming the greatest energy transfer between two black bodies ($\in_{eff} = 1$) and close proximity between the heater and the membrane (F=1), this equation can be simplified to $\Delta E = \sigma A(T_A^4 - T_B^4)$. Considering a test membrane of m² at an initial temperature of 20°C, the maximum radiative energy transfer between the membrane and a heat source at 200°C would be 0.012 W.

Compared to the 0.44 W estimated heat source of a thin-film heater used to actuate the valves, radiation can be neglected.

Valve actuation

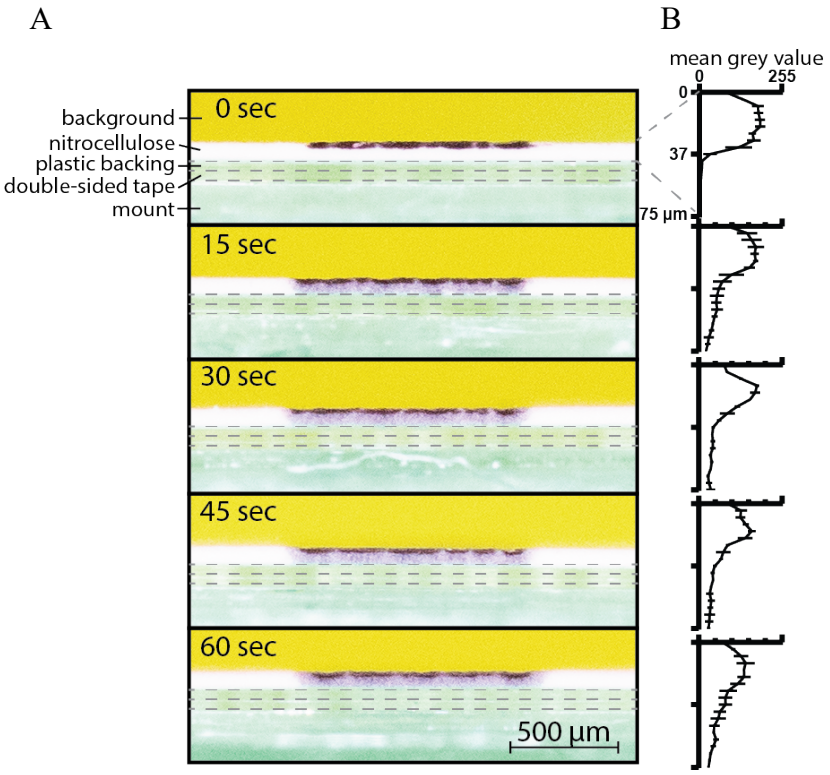

Figure S2: Distribution of wax-ink through partially closed valves. (A) Images of edge of 0.1 mm valve printed onto nitrocellulose membrane and heated for 0-60 seconds to demonstrate. (B) The mean grey value plotted against membrane depth. Error bars indicate standard error (n=3).

Due to convective heat transfer, there is a measurable difference in temperature along the length (x-axis) of the valve. The Multiphysics model was simplified to include a free stream velocity of 0.1 m/s in only one direction. In reality, there is multi-directional air flow, however, given the locations of HVAC vents in our laboratory, it is reasonable to assume a predominant air flow in one direction. When laminar air flow is included in the model, the temperature of wax at the edge (closest to the air inlet) of the membrane is several degrees higher than the wax at the midpoint of the valve (supplemental information). As expected, when this air velocity is much higher (1 m/s) the temperature of the wax never reaches its melting temperature and when the air velocity is negligible, the wax heats rapidly. Evaporative heat loss was included in the model because water samples were observed to evaporate from the membrane during empirical testing of valve opening conditions. When evaporative heat loss is neglected from the model, the temperature difference between the middle and the edge of the wax valve increases slightly. As expected, the entire valve heats faster than when evaporative heat loss is neglected due to latent heat of evaporation. The several degree temperature difference between the middle and edge of a heated valve is consistent with both the IR imaging results and observations of flow past the edge of a valve (Figure S5A).

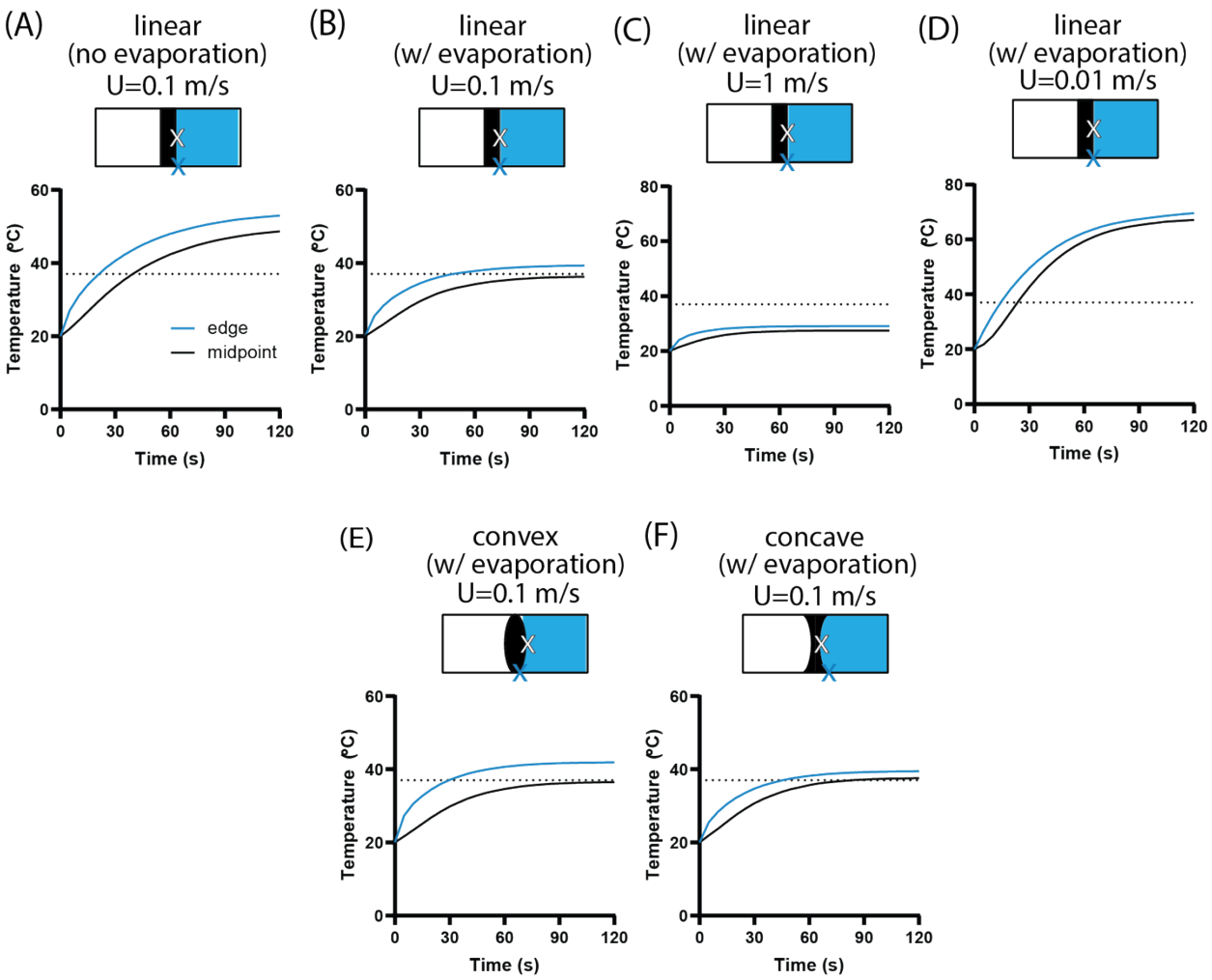

Figure S3: Simulated temperature difference between the midpoint and edge of wax valves.

The dotted line depicts the temperature when paraffin wax begins to melt. (A) When heat loss is only from convective heat transfer, there is a several degree difference in temperature between the edge and the middle of a linear valve on the bottom face. (B) When evaporative heat loss is included, the temperature difference reduces. (C) With greater convection, the wax never reaches the melting temperature. (D) With negligible convection, there is still a temperature difference between the middle and edge. (E) A convex valve has the greatest temperature difference while (F) a concave valve has the smallest temperature difference.

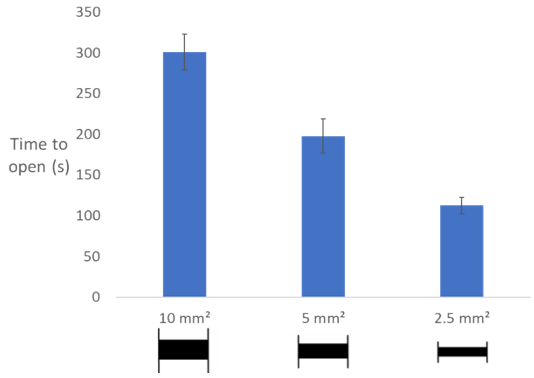

Figure S4: Time for fluid to begin flowing through opposite side of wax valve after heating.

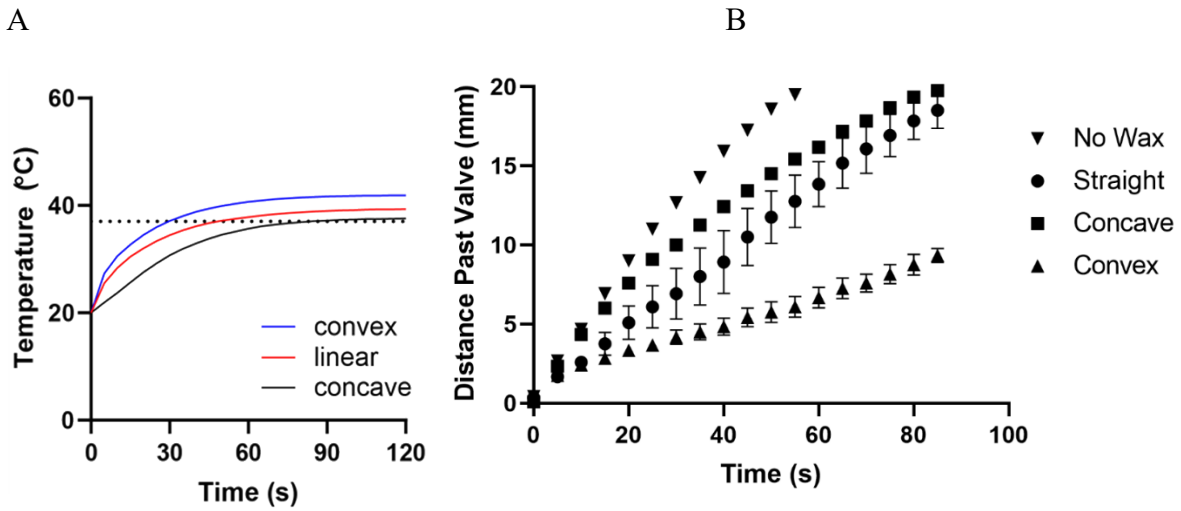

Figure S5: (A) Simulated temperature at thinnest region of valve. The narrowest regions of convex valves (along edges of the channel) heat faster than linear and concave valves and would likely open first. Dotted line depicts temperature that paraffin wax begins to melt. (B) Extended data describing flow rate past different types of valves compared to no valve (n = 3 and error bars represent standard error of the mean).

MATLAB Model of Fluid Flow

Here, the nitrocellulose membrane was assumed to be a two-dimensional system with four edges, and the effects of gravity were neglected. One edge was assumed to be in contact with a water reservoir; here, a Dirichlet boundary condition was applied.[52] On the other three edges, a Neumann boundary condition with no flux was applied.[53]

In addition to these boundary conditions, this model assumed that air inside the nitrocellulose could only travel through the thin membrane layer and escape from the edges, since it was sealed on the top surface, changing the effective porosity of the nitrocellulose and thus the gas permeability of the medium.[54] Gas transport in a porous medium can be described by a corollary to Darcy's law:[55]

$$J = -\frac{K}{kT}\nabla p ,$$

where *K* is gas permeability and ∇p is the pressure gradient. This equation differs from Darcy's law in that *T*, temperature, replaces liquid viscosity. Furthermore, since the Lucas-Washburn equation can be derived from Darcy's law,[4] the velocity of gas in a porous medium can likewise be described with a relationship similar to the Lucas-Washburn equation:

$$L = C\sqrt{t},$$

where *C* is a constant based on material, gas, and temperature properties of the system. Since the nitrocellulose membrane is sealed on the top and bottom surfaces, the velocity of air traveling through it was parallel to the direction of the pressure gradient at each point on the liquid fluid front. The air in the center of the membrane took a much longer time to escape from the membrane than air closer to the edges, decreasing the permeability of the membrane to liquid traveling through it. Therefore, the diffusivity factor *D(ϑ)* from the Richard's equation was modified to include a function, *f(x)*, with a high boundary value and a steep decrease in value approaching the center of the membrane. *F(x)* is an exponential function fit to the experimental data for the purpose of this model. This value was substituted into Richard's equation and solved to produce flow rate patterns for wax-free systems shown in Figure 3 B, C, D.

$$D'(\theta) = D(\theta) + f(x)$$

To calculate the velocity at specific distance points, a second-order numerical method was used to interpolate the data comprising this mathematical model to get finer data points. The derivative of the equation was taken at the distance points of interest (in this case, 10 mm and 15 mm) to calculate the bulk flow velocity at those locations (0.345 mm/s and 0.263 mm/s, respectively). Two different interpolation methods produced identical velocity data.

Extended flow rate data:

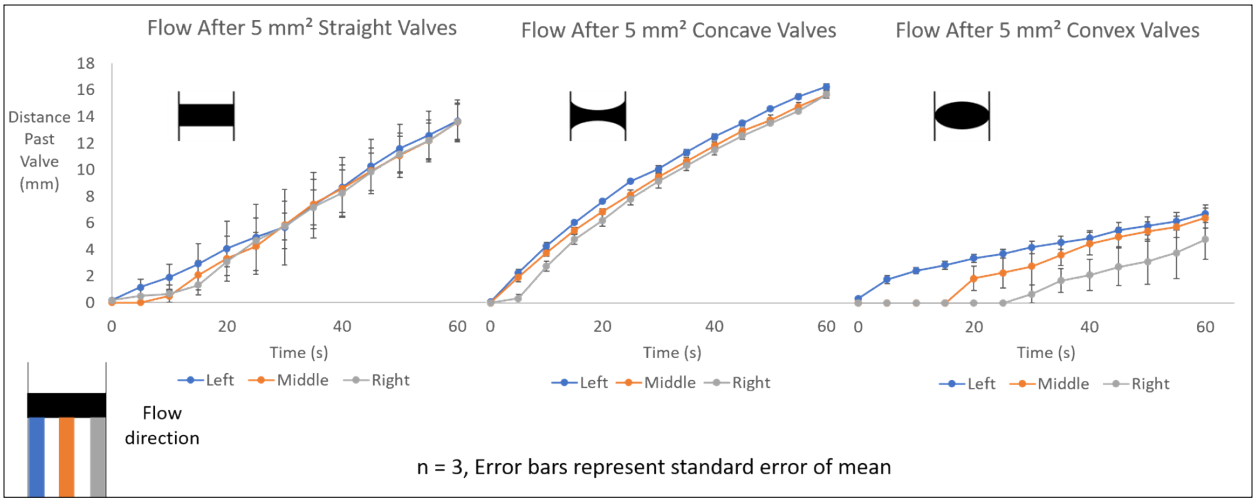

Figure S6: Flow rates for fluid through left edge, middle, and right edge of nitrocellulose membranes past 5 mm2 straight, concave, and convex valves.

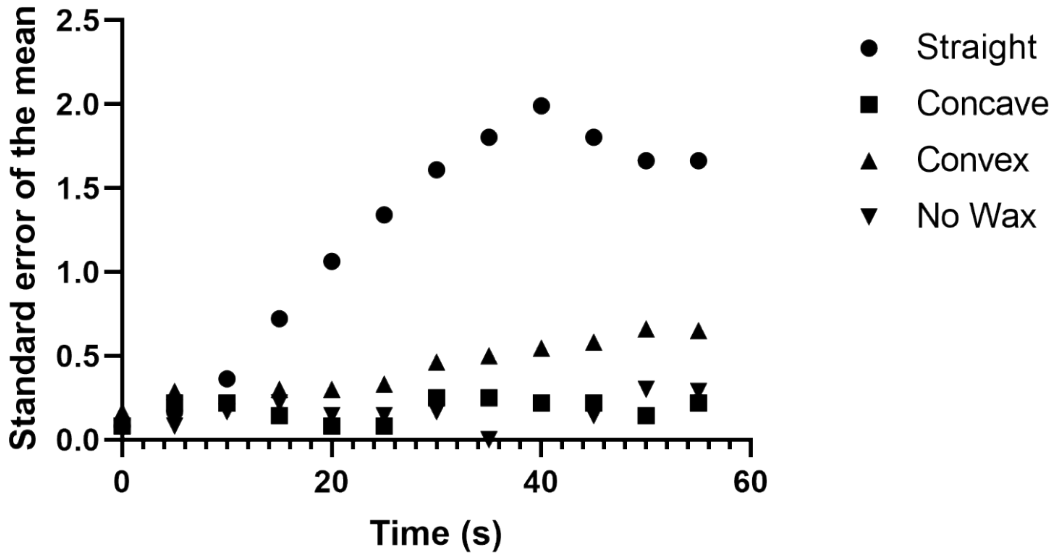

Figure S7: Standard error of the mean plotted for each time point in Figure 3A.

Table S2: One-way ANOVA with Tukey's multiple comparisons test of standard error of the mean of flow distances over time past different valves.

Tukey's multiple comparisons test	Mean Diff.	95.00% CI of diff.	Below threshold?	Summary	Adjusted P Value
Concave vs. Straight	0.5077	-0.2108 to 1.226	No	ns	0.2294
Concave vs. Convex	-0.8430	-1.561 to -0.1245	Yes	*	0.0179
Concave vs. No wax	1.927	1.209 to 2.646	Yes	****	<0.0001
Straight vs. Convex	-1.351	-2.069 to -0.6322	Yes	***	0.0002
Straight vs. No wax	1.420	0.7011 to 2.138	Yes	***	0.0001
Convex vs. No wax	2.770	2.052 to 3.489	Yes	****	<0.0001

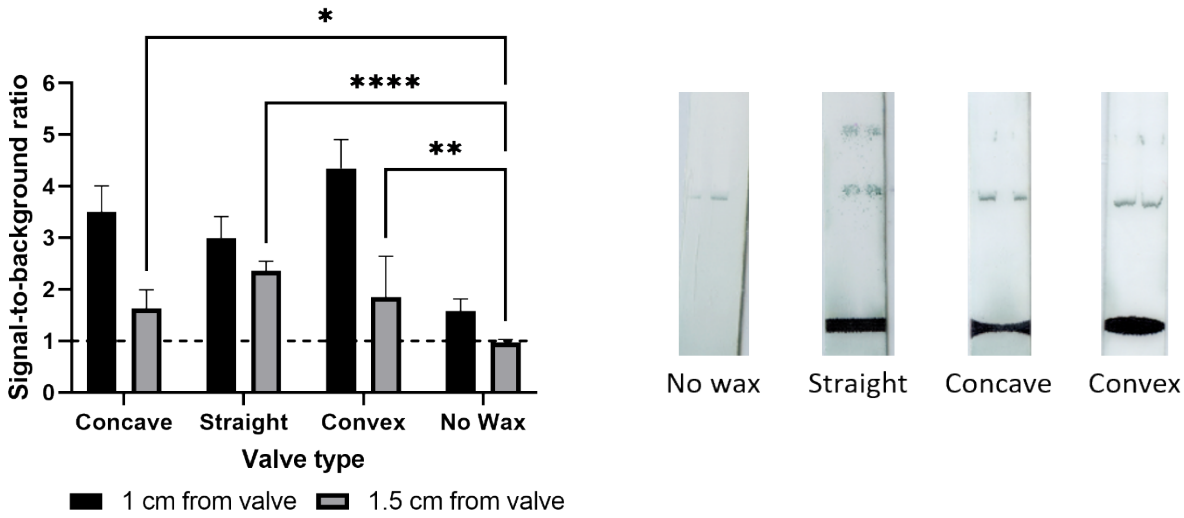

Figure S8: A. Signal-to-background ratio for test spot signal 10 and 15 mm downstream of the valve location. Error bars represent standard deviation. A two-way ANOVA with multiple comparisons was performed on this dataset to compare signal formation at test spots 15 mm downstream of the valves. B. Representative images of triplex assays without a wax valve and with straight, concave, and convex valves.

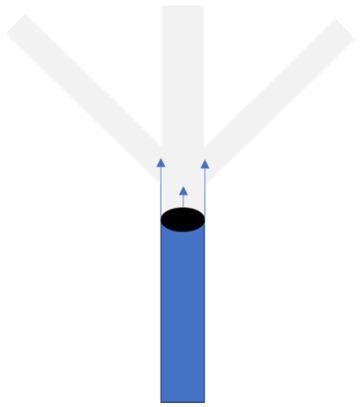

Figure S9: An example assay design using convex valves and multiple side outlets for controlled release and slow delivery of fluid.

Microscopic Fluid Analysis with 100 nm Particles

Analysis of 100 nm nanoparticles shows velocity distributions on the same order of magnitude as the 400 nm particles (Figure S7). Interestingly, histograms of 100 nm particle velocity did not have as significant of high-velocity tails as the 400 nm particle histograms. This could potentially be due to the signal produced by the 100 nm smaller particles moving at higher velocities being too small to be captured by the µPIV analysis. Contrary to the 400 nm particles, however, the motion of individual particles was not visible; therefore, it is not possible to see whether the vector field matches the particle flow pattern. The inability to see visible particles prevents us from visually confirming the analysis.

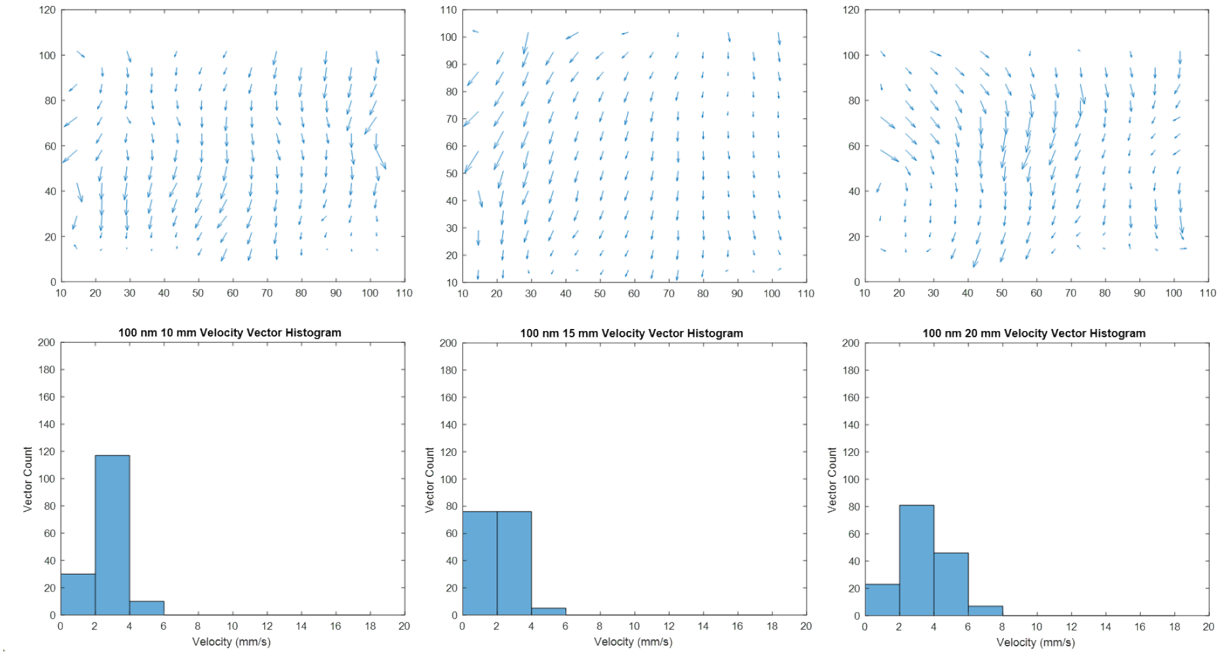

Figure S10: Vector fields and histograms of velocity distribution for 100 nm particles in nitrocellulose.